Symmetry potentials and in-medium nucleon-nucleon cross sections within the Nambu–Jona-Lasinio model in relativistic impulse approximation

Si-Na Wei,[*] Rong-Yao Yang ⬤, Jing Ye, Niu Li, and Wei-Zhou Jiang ⬤[†]

School of Physics, Southeast University, Nanjing 211189, China

In the relativistic impulse approximation (RIA), we study symmetry potentials and in-medium nucleon-nucleon (NN) cross sections with the Nambu–Jona-Lasinio (NJL) model that features chiral symmetry. The chiral symmetry that plays a fundamental role in the nonperturbative physics in the strong interaction is anticipated to add restrictive effects on the symmetry potentials and in-medium NN cross sections. For comparison, we also perform the study with the usual relativistic mean-field (RMF) model. The numerical results with the NJL and RMF models are similar at saturation density and below, since *a priori* fit was made to saturation properties. With the increase of nuclear density, the chiral symmetry starts to be restored partially in the NJL model, resulting in the explicit fall of the scalar density. In a large energy span, the symmetry potential acquires a significant rise for the partial restoration of the chiral symmetry, compared to the one with the RMF model. It is found that the in-medium NN cross sections in the RIA with the NJL and RMF models both increase with the density in the energy region interested in this study, whereas those with the NJL model increase sharply as long as a clear chiral symmetry restoration takes place. The different tendency of observables in density can be transmitted to the different energy dependence in the RIA. The NJL model is shown to have characteristic energy-dependent symmetry potentials and NN cross sections beyond saturation point, apart from the RMF models.

I. INTRODUCTION

Heavy-ion reaction experiments are indispensable to extract the nuclear equation of state (EOS) of asymmetric matter in various density regions. In-medium nucleon-nucleon (NN) cross sections are key inputs of reaction models, such as Glauber models [1] and various transport models [2]. Up to now, though great success in constraining the EOS of asymmetric matter has been achieved [3,4], considerable uncertainty of the EOS at high densities remains due to the facts that the extraction of the EOS from data relies actually on various models and that the solution of highly nonlinear nuclear in-medium problems is subject to the many-body theory with various approximations. In particular, the large uncertainty exists eminently in the density dependence of the symmetry energy, which is one of two important ingredients of nuclear EOS of asymmetric matter. In fact, the uncertainty of the symmetry energy is closely associated with the rather flexible isovector part of nucleon potentials, i.e., the symmetry potential. Since the density dependence of the symmetry energy plays a very important role in nuclear physics and astrophysics [5–7], the constraint on the uncertainty in the symmetry energy and symmetry potential has received enormous attention in past two decades [4,7–14]. It has been recognized that the theoretical uncertainty in extracting the density dependence

of the symmetry energy from data of heavy-ion reactions can be largely ascribed to the poor knowledge and premature treatment of the isospin-dependent in-medium NN cross sections [11]. For instance, in most Glauber calculations, only the isospin averaged free-space nucleon-nucleon cross section is used. Indeed, in spite of the well-determined NN cross section in free space, the in-medium NN cross section is phenomenological or model dependent [15–26].

Due to the interplay between the uncertainty of the EOS and the complexity of the in-medium interactions, it is far off straightforward to derive simultaneously the symmetry potential and in-medium NN cross sections microscopically or simply by model extrapolations with consistency. For this reason, we seek help of first principles with the following two considerations. First, we will highly value the role of chiral symmetry in nuclear mean fields and NN cross sections, since the chiral symmetry property takes part to acquire most of the mass for nucleons and to recover the chiral symmetry partially in the dense medium. Second, it is necessary to derive in-medium NN cross sections consistent with the mean fields of nuclear matter that determine the symmetry potential. With these considerations, in this work we will deal with the symmetry potential and in-medium NN cross sections in the relativistic impulse approximation (RIA) that is connected to the mean fields obtained from the chiral model.

In popular chiral models such as the linear-σ and Nambu–Jona-Lasinio (NJL) models [27–29], the chiral condensate on the nucleonic level is related to the scalar field. Therefore, the partial restoration of chiral symmetry in the nuclear medium

---

[*]471272396@qq.com

[†]Corresponding author: wzjiang@seu.edu.cn

brings the effect on the scalar mean field and consequently the in-medium NN cross sections. This will eventually modify the symmetry energy extracted from heavy-ion reaction data. In this work, we will adopt the NJL model to produce the mean fields. The original NJL model was established as a theory for compound particles with constituent nucleons [28]. In the past, the NJL model has been widely used on a quark level [30–37] and a nucleonic level [38–45]. On the nucleonic level, the original NJL model cannot produce saturation properties of nuclear matter. Similar to the σ model [29], a scalar-vector interaction was introduced to cure this problem, and the NJL model has been extended to include other interactions respecting the chiral symmetry [42–45]. We will start with the nucleonic NJL model that can reproduce the saturation properties.

The RIA combines the Dirac decomposition of scattering amplitudes and nuclear scalar and vector densities with the experimental data. The optical potentials obtained from the RIA reproduced the analyzing power and spin-rotation parameter in proton-nuclei scatterings successfully [46–48], whereas the standard nonrelativistic optical models failed to describe experimental data for spin observables [49,50]. Later, the RIA was also extended to the relative low-energy nucleon-nuclei elastic scatterings [51–53]. The RIA success interprets the importance of the relativistic dynamics. In the past, the RIA was also used to study the symmetry potentials [12,13,54,55] and in-medium NN cross sections [23]. Although the scattering amplitudes can provide a constraint on the symmetry potential in the RIA, it is generally known that the energy and density dependence of the symmetry potential obtained from many other approaches relies actually on specific parametrizations [7,12–14]. As the symmetry potential and in-medium NN cross sections diversify for various in-medium interactions in nuclear models and approaches, it is rather advantageous to study them with the RIA in a unified manner. In this work, we are thus motivated to revisit the symmetry potential and in-medium NN cross sections uniformly in the RIA based on the NJL model that follows the chiral symmetry. For comparison, we will also perform the study with the usual relativistic mean-field (RMF) model.

The paper is organized as follows. In Sec. II, we briefly introduce formalism and approaches used in this work. They include a brief RMF formalism, the NJL model, the RIA, and the in-medium NN cross sections and relevant quantities. Results and discussion are presented in Sec. III. A summary is finally given in Sec. IV.

II. FORMALISM

A. Relativistic mean-field theory

The original version of RMF model is the Walecka model [56], which only contains scalar and vector mesons to provide the medium-range attraction and short-range repulsion between the nucleons, respectively. Since the incompressibility of Walecka model is too large, Boguta and Bodmer introduced the nonlinear self-interactions of the σ meson to bring down the incompressibility reasonably [57]. For studying the isospin-asymmetric nuclei, the isovector (ρ) meson was later invoked to account for the isospin dependence of the

nuclear force [58]. To eliminate the scalar potential instability caused by the nonlinear self-interaction of the σ meson at high density, Bodmer and later Sugahara and Toki took the nonlinear self-interaction of the ω meson into account [59,60]. Due to the uncertainty of the symmetry energy, the interaction between the ω and ρ mesons was later involved in a full Lagrangian [61]:

$$
\begin{aligned}
\mathcal{L} &= \bar{\psi}[\gamma_\mu(i\partial^\mu - g_\omega\omega^\mu - g_\rho\tau_3 b^\mu) - (M - g_\sigma\sigma)]\psi \\
&+ \tfrac{1}{2}(\partial_\mu\sigma\,\partial^\mu\sigma - m_\sigma^2\sigma^2) - \tfrac{1}{4}F_{\mu\nu}F^{\mu\nu} + \tfrac{1}{2}m_\omega^2\omega_\mu\omega^\mu \\
&- \tfrac{1}{4}B_{\mu\nu}B^{\mu\nu} + \tfrac{1}{2}m_\rho^2 b_\mu b^\mu - \tfrac{1}{3}g_2\sigma^3 - \tfrac{1}{4}g_3\sigma^4 \\
&+ \tfrac{1}{4}c_3(\omega_\mu\omega^\mu)^2 + 4\Lambda_V g_\rho^2 g_\omega^2 \omega_\mu\omega^\mu b_\mu b^\mu,
\end{aligned}
\tag{1}
$$

where g_i and m_i with $i = \sigma, \omega, \rho$ are the meson-nucleon coupling constants and the meson masses, respectively. g_2 and g_3 are the coupling constants of the nonlinear self-interaction of the σ meson. c_3 is the coupling constant of the nonlinear self-interaction of the ω meson. $F_{\mu\nu}$ and $B_{\mu\nu}$ are the strength tensors of ω and ρ mesons, respectively

$$
F_{\mu\nu} = \partial_\mu\omega_\nu - \partial_\nu\omega_\mu, \quad B_{\mu\nu} = \partial_\mu b_\nu - \partial_\nu b_\mu.
\tag{2}
$$

With this Lagrangian, a nicely fit RMF parametrization is the FSUGold by Todd and Piekarewicz [62]. The equations of motion for the nucleon and meson are actually the Euler-Lagrange equations from above Lagrangian. In the RMF approximation, they are given as follows:

$$
[i\gamma^\mu\partial_\mu - g_\omega\gamma^0\omega_0 - g_\rho\gamma^0 b_0\tau_3 - (M - g_\sigma\sigma)]\psi = 0,
\tag{3}
$$

$$
m_\sigma^2\sigma = g_\sigma\rho_S - g_2\sigma^2 - g_3\sigma^3,
\tag{4}
$$

$$
m_\omega^2\omega_0 = g_\omega\rho_B - c_3\omega_0^3 - 8\Lambda_V g_\rho^2 g_\omega^2 b_0^2\omega_0,
\tag{5}
$$

$$
m_\rho^2 b_0 = g_\rho\rho_3 - 8\Lambda_V g_\rho^2 g_\omega^2 \omega_0^2 b_0,
\tag{6}
$$

where $\rho_S = \langle\bar{\psi}\psi\rangle$ and $\rho_B = \langle\bar{\psi}\gamma^0\psi\rangle$ are the scalar density and baryon density respectively. $\rho_3 = \langle\bar{\psi}\gamma^0\tau_3\psi\rangle = \rho_p - \rho_n$ is the difference between the proton and neutron densities. For a given baryon density ρ_B and isospin asymmetry parameter $\delta = (\rho_n - \rho_p)/\rho_B$, the set of coupled equations can be solved self-consistently by iterative methods.

B. Nambu–Jona-Lasinio model of nucleonic level

On the nucleonic level, the extended NJL which contains scalar, vector, and scalar-vector interactions can successfully produce the saturation property [38]. For asymmetric nuclear matter, it is reasonable to include the isovector and isovector-scalar interactions [42,43]. The Lagrangian is written as

$$
\begin{aligned}
\mathcal{L} &= \bar{\psi}(i\gamma_\mu\partial^\mu - m_0)\psi + \frac{G_S}{2}[(\bar{\psi}\psi)^2 - (\bar{\psi}\gamma_5\tau\psi)^2] \\
&- \frac{G_V}{2}[(\bar{\psi}\gamma_\mu\psi)^2 + (\bar{\psi}\gamma_\mu\gamma_5\psi)^2] \\
&+ \frac{G_\rho}{2}[(\bar{\psi}\gamma_\mu\tau\psi)^2 + (\bar{\psi}\gamma_\mu\gamma_5\tau\psi)^2] \\
&+ \frac{G_{SV}}{2}[(\bar{\psi}\psi)^2 - (\bar{\psi}\gamma_5\tau\psi)^2][(\bar{\psi}\gamma_\mu\psi)^2 + (\bar{\psi}\gamma_\mu\gamma_5\psi)^2] \\
&+ \frac{G_{\rho S}}{2}[(\bar{\psi}\gamma_\mu\tau\psi)^2 + (\bar{\psi}\gamma_\mu\gamma_5\tau\psi)^2][(\bar{\psi}\psi)^2 - (\bar{\psi}\gamma_5\tau\psi)^2],
\end{aligned}
\tag{7}
$$

where the m_0 is the bare nucleon mass and G_S, G_V, G_{SV}, G_ρ, and $G_{\rho S}$ are the scalar, vector, scalar-vector, isovector, and isovector-scalar coupling constants, respectively. In the RMF approximation, the Lagrangian can be simplified to be

$$\mathcal{L} = \mathcal{L}_0 + \mathcal{L}_{IV} = \bar{\psi}[i\gamma_\mu \partial^\mu - M^* - \gamma^0 \Sigma]\psi - U, \quad (8)$$

where M^*, Σ, and U are respectively defined as

$$M^* = m_0 - (G_S + G_{SV}\rho_B^2 + G_{\rho S}\rho_3^2)\chi_S, \quad (9)$$

$$U = \tfrac{1}{2}(G_S\chi_S^2 - G_V\rho_B^2 - G_\rho\rho_3^2 + 3G_{SV}\chi_S^2\rho_B^2 + 3G_{\rho S}\rho_3^2\chi_S^2), \quad (10)$$

$$\Sigma = G_V\rho_B + G_\rho\rho_3\tau_3 - G_{SV}\chi_S^2\rho_B - G_{\rho S}\rho_3\chi_S^2\tau_3, \quad (11)$$

with

$$\chi_S = -\sum_{i=p,n}\int_{k_{F_i}}^{\Lambda}\frac{d^3k}{(2\pi)^3}\frac{M^*}{\sqrt{k^2 + M^{*2}}}. \quad (12)$$

Here, Eq. (9) is the gap equation for the nucleon effective mass in the NJL model, and the bare nucleon mass m_0 is obtained from the relation $m_\pi^2 f_\pi^2 = m_0\chi_S^{\text{vac}}$. In addition to the small m_0 that breaks the chiral symmetry explicitly, the dynamic mass, generated from the vacuum scalar condensate χ_S, breaks the chiral symmetry predominately, which is known as the spontaneous breaking of chiral symmetry. As the baryon density increases, the Fermi momentum will be approaching the momentum cutoff Λ, which is necessarily introduced to regularize the high-momentum behavior in the calculation, and the dynamic mass decreases to vanishing at the critical density with $k_F = \Lambda$ in symmetric matter where the chiral symmetry restoration takes place. More details of the chiral symmetry restoration in nuclear matter can be referred to Ref. [40]. In order to check the effect of the chiral restoration whose critical density is determined by the momentum cutoff, we employ two different momentum cutoffs, 350 and 400 MeV, which correspond to the critical densities $2.37\rho_0$ and $3.53\rho_0$ ($\rho_0 = 0.16$ fm^{-3}), respectively. The parameters for the NJL350 and NJL400 can be found in our previous works [43,63]. The incompressibility values are 262 and 296 MeV for NJL350 and NJL400, respectively. The symmetry energy and the slope of symmetry energy with various momentum cutoffs are set to be 31.6 and 50.0 MeV by adjusting G_ρ and $G_{\rho S}$, respectively.

C. Relativistic impulse approximation

In proton-nucleus scattering, the scattering process can be approximately treated as incident proton scattered by each of the nucleons in the target nucleus by neglecting the impact of incident particle to the mean fields. Therefore, the Dirac optical potential can be approximated as [46,47]

$$\tilde{U}_{\text{opt}}(q) = -\frac{4\pi i p_{\text{lab}}}{M}\langle\bar{\Psi}|\sum_{n=1}^{A}e^{i\vec{q}\cdot\vec{r}(n)}\hat{F}(q,n)|\Psi\rangle, \quad (13)$$

where p_{lab} and M are the laboratory momentum and mass of the incident nucleon, respectively. Ψ is the ground state of target nucleus. $\hat{F}$ is Lorentz-invariant NN scattering amplitudes and can be decomposed into five components:

$$\hat{F} = F_S + F_V\gamma_1^\mu\gamma_{2\mu} + F_T\sigma_1^{\mu\nu}\sigma_{2\mu\nu} + F_P\gamma_1^5\gamma_2^5 + F_A\gamma_1^5\gamma_1^\mu\gamma_2^5\gamma_{2\mu}, \quad (14)$$

where F_S, F_V, F_T, F_P, and F_A are the scalar, vector, tensor, pseudoscalar, and axial vector amplitudes, respectively. For the spin-saturated nucleus, $\hat{F}$ only contains scalar (F_S), vector (F_V), and tensor (F_T) terms. Since the tensor term of the scattering amplitude is small, the Dirac optical potential can be approximately written as

$$\tilde{U}_{\text{opt}}(q) = -\frac{4\pi i p_{\text{lab}}}{M}[F_S(q)\tilde{\rho}_S(q) + \gamma^0 F_V(q)\tilde{\rho}_B(q)]. \quad (15)$$

For a nucleon scattering off finite nuclei, the momentum transfer q between nucleon and finite nuclei is important for understanding the scattering angle-dependent physical quantities (such as differential cross sections). When the target is infinite nuclear matter, the scalar and vector densities are constant in coordinate space. This means only the forward NN scattering amplitudes [$F_S(q = 0)$ and $F_V(q = 0)$] survive. Therefore, the Dirac optical potential is simplified as [46,47]

$$U_{\text{opt}} = -\frac{4\pi i p_{\text{lab}}}{M}[F_S\rho_S + \gamma^0 F_V\rho_B]. \quad (16)$$

The forward NN elastic scattering amplitudes F_S and F_V [46,47] have been determined directly from the experimental NN phase shifts [64], and have been successfully used to describe pA elastic scattering with incident energies above 400 MeV [48]. In this work, we apply these free-space NN elastic scattering amplitudes to perform the RIA study in the medium. As pointed out in Ref. [64], some resonance-like noise may exist in the data at nucleonic kinetic energies between 650 and 800 MeV. The RIA can also project the inelastic noise approximately onto the Dirac optical potentials, since the inelastic scattering amplitudes, albeit involving a resonant state mass larger than the nucleon counterpart, do not violate the Lorentz decomposition in Eq. (14) and the RIA structure in Eqs. (15) and (16). Consequently, our RIA results may include some inelastic ingredients from the data with the resonance-like noise in the certain energy region. Below 400 MeV, one can use the NN elastic scattering amplitude of relativistic Love-Franey model developed by Murdock and Horowitz [51,52]. ρ_S and ρ_B are the spatial scalar and vector densities of infinite nuclear matter,

$$\rho_{S,i} = \int_0^{k_{Fi}}\frac{d^3k}{(2\pi)^3}\frac{M^*}{\sqrt{M^{*2} + k^2}},$$

$$\rho_{B,i} = \frac{k_{Fi}^3}{3\pi^2}, \; i = n, p. \quad (17)$$

When the density-dependent effective mass M^* of nucleons is obtained from nuclear models, the scalar density can be calculated from Eq. (17) directly. The Dirac optical potential can be expressed in terms of scalar and vector optical potentials:

$$U_{\text{opt}} = U_S^{\text{tot}} + \gamma_0 U_0^{\text{tot}},$$

$$U_S^{\text{tot}} = U_S + iW_S, \; U_0^{\text{tot}} = U_0 + iW_0, \quad (18)$$

where U_S, W_S, U_0, and W_0 are respectively real scalar, imaginary scalar, real vector, and imaginary vector optical potentials.

D. Symmetry potential and in-medium NN cross section

In order to study nuclear symmetry potential, the nucleon mean free path (MFP), and in-medium NN cross section, it is useful to derive the Schrödinger equivalent potential (SEP) from the Dirac equation. The Dirac equation can be decomposed into two equations for the small and large components of the Dirac spinor. By eliminating the small component of the Dirac spinor, one can obtain a Schrödinger-like equation for the large component. To obtain the SEP, there are two schemes by Jaminon et al. [65] and Hama et al. [66]. Regardless of the small Darwin term and Coulomb potential, the SEP following the Jaminon's definition (denoted by "J") is written as [65]

$$U_{\text{sep},J}^{\text{tot}} = U_S^{\text{tot}} + U_0^{\text{tot}} + \frac{U_S^{\text{tot}2} - U_0^{\text{tot}2}}{2M} + \frac{U_0^{\text{tot}}E_{\text{kin}}}{M}, \quad (19)$$

with $U_{\text{sep},J}^{\text{tot}} = U_{\text{sep},J} + iW_{\text{sep},J}$. E_{kin} is the nucleon kinetic energy. In the Hama's definition [66], the SEP (denoted by "H") is given as

$$U_{\text{sep},H}^{\text{tot}} = \left[U_S^{\text{tot}} + U_0^{\text{tot}} + \frac{U_S^{\text{tot}2} - U_0^{\text{tot}2}}{2M} + \frac{U_0^{\text{tot}}E_{\text{kin}}}{M} \right] \frac{M}{E}$$
$$= \frac{1}{2E} \left[2E U_0^{\text{tot}} + 2M U_S^{\text{tot}} + U_S^{\text{tot}2} - U_0^{\text{tot}2} \right], \quad (20)$$

with $E = E_{\text{kin}} + M$. Numerically, $U_{\text{sep},H}^{\text{tot}}$ equals $U_{\text{sep},J}^{\text{tot}}M/E$. Equations (19) and (20) can overestimate and underestimate the SEP at high energies, respectively. As seen below, these two expressions actually give rise to the the same nucleon MFPs and NN cross sections. By applying the SEP, the real and imaginary symmetry potentials are obtained as

$$U_{\text{sym}} = \frac{U_{\text{sep}}^n - U_{\text{sep}}^p}{2\delta},$$
$$W_{\text{sym}} = \frac{W_{\text{sep}}^n - W_{\text{sep}}^p}{2\delta}, \quad (21)$$

where U_{sym} is the well-known Lane potential [67]. Using the dispersion relation [68] and assuming a complex momentum $k = k_R + ik_I$, the nucleon MFP can be obtained as [23]

$$\lambda_i = \frac{1}{2k_I} = \frac{\sqrt{2}}{2} \Big\{ - \big(E^2 - M^2 - 2MU_{\text{sep}}^i\big)$$
$$+ \big[\big(E^2 - M^2 - 2MU_{\text{sep}}^i\big)^2 + \big(2MW_{\text{sep}}^i\big)^2\big]^{1/2} \Big\}^{-1/2}. \quad (22)$$

Note that $\lambda_{i,J} = \lambda_{i,H}$ because of the relation $U_{\text{sep},H}^{\text{tot}} = U_{\text{sep},J}^{\text{tot}}M/E$. Thus, we neglect the subscripts J and H in the following. The nucleon MFP can also be expressed as the length of the unit volume defined by the matter density and the NN cross section [69]. In this case, the nucleon MFP reads

$$\lambda_i = (\rho_p \sigma_{ip}^* + \rho_n \sigma_{in}^*)^{-1}, \quad (23)$$

where σ^*'s are in-medium NN scattering cross sections, and ρ_p and ρ_n are the proton and neutron densities, respectively. At some circumstances where the isospin dependence is small,
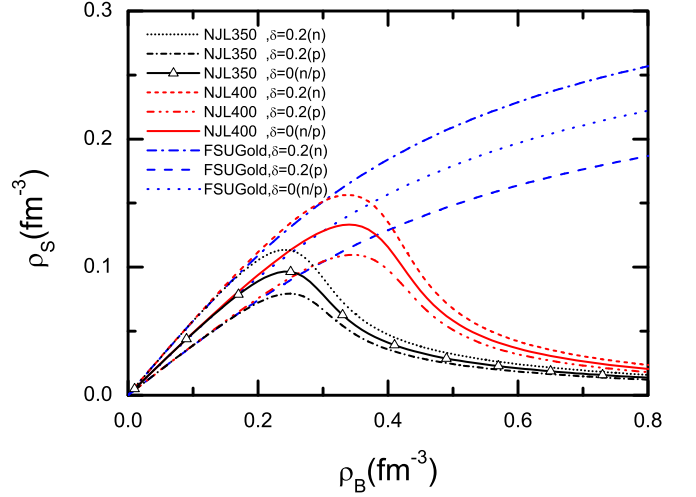

FIG. 1. The neutron and proton scalar densities as functions of density with parametrizations of the NJL model and FSUGold. n and p are abbreviations of neutron and proton, respectively, and n/p means neutron or proton at $\delta = 0$.

the in-medium NN cross sections can be obtained from the above equation. It is useful to define two quantities [23],

$$\tilde{\lambda}^{-1} = \frac{1}{2\delta}\left(\frac{1}{\lambda_n} - \frac{1}{\lambda_p}\right), \quad \tilde{\Lambda}^{-1} = \frac{1}{2}\left(\frac{1}{\lambda_n} + \frac{1}{\lambda_p}\right). \quad (24)$$

With Eqs. (23) and (24), in-medium NN cross sections can be obtained as

$$\sigma_{pp}^* = (\tilde{\Lambda}^{-1} + \tilde{\lambda}^{-1})/\rho_B, \quad \sigma_{np}^* = (\tilde{\Lambda}^{-1} - \tilde{\lambda}^{-1})/\rho_B, \quad (25)$$

by assuming $\sigma_{pp}^* = \sigma_{nn}^*$ on the fact that $\tilde{\Lambda}$ and $\tilde{\lambda}$ were proved to be approximately independent of the isospin asymmetry of the medium at high energies which is much larger than the Fermi momentum [23]. The in-medium neutron-neutron and proton-proton scattering cross sections are thus equal by neglecting the small charge symmetry-breaking effect [70] and small isospin-dependent Pauli blocking effects at high energies in asymmetric nuclear matter. Such an inference will become weak at low energies or at high densities where the isospin-dependent Pauli blocking arises in $\tilde{\Lambda}$ and $\tilde{\lambda}$ for the comparable Fermi momentum and kinetic energy E_{kin}.

III. RESULTS AND DISCUSSION

In the RIA, the scalar and vector densities, associated respectively with the scalar and vector potentials which represent the relativistic dynamics, are two important components to work out the Dirac optical potentials. The scalar density of nuclear matter is calculated with Eq. (17) where the nucleon effective mass M^* is obtained by solving the mean fields self-consistently in relativistic models. Here, we adopt the NJL model [43] and a nicely-fit RMF parametrization FSUGold [62] for comparison to check the effect of chiral symmetry on observables. Figure 1 shows the neutron and proton scalar densities as functions of baryon density ρ_B. The isospin asymmetry $\delta = (\rho_n - \rho_p)/\rho_B$ is taken to be 0 and 0.2. At $\delta = 0.2$, the neutron scalar density is always above the proton scalar
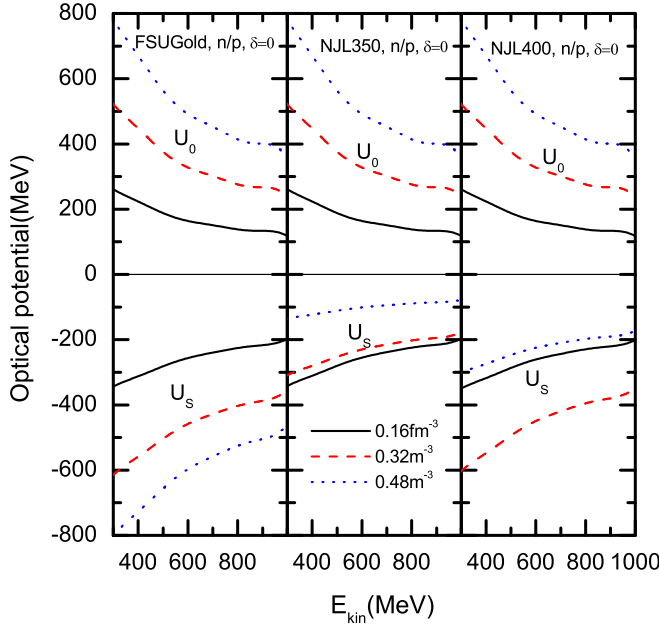
FIG. 2. Real parts of the scalar (U_S) and vector (U_0) Dirac optical potentials for neutrons and protons with various parametrizations at $\rho_B = 0.16, 0.32, 0.48$ fm^{-3} as functions of the nucleon kinetic energy.
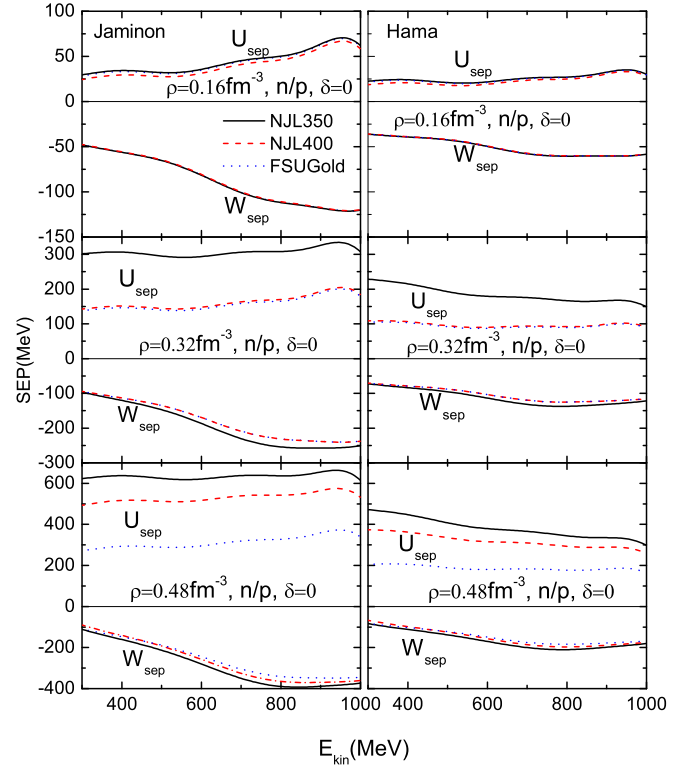

FIG. 3. Real and imaginary parts of Schrödinger equivalent potentials as functions of nucleon kinetic energies in symmetric matter at different densities. The real and imaginary parts are above and below zero, respectively. The results in the left and right panels are calculated with Eqs. (19) and (20), respectively.

density for the higher Fermi surface, as shown in Fig. 1. We see that the scalar density with the FSUGold increases with increasing the baryon density. It is, however, interesting to find that the scalar density with the NJL model first increases and then decreases with increasing the baryon density. This result, distinct from common nuclear models, is due to the characteristics of chiral symmetry in the NJL model. With the increase of density, the chiral symmetry undergoes gradual restoration, which is reflected by a more rapid dropping of the nucleon effective mass. When the density is close to the critical density for chiral symmetry restoration, the nucleon loses its mass down to the chiral limit, and the scalar density of nuclear matter becomes small. Since the critical density with the NJL350 is less than that with the NJL400, the scalar density with the NJL350 starts to decrease at a density lower than the one with the NJL400.

With employing the above neutron and proton scalar densities and the forward NN scattering amplitudes, the scalar and vector Dirac optical potentials for neutrons and protons in nuclear matter are obtained directly by virtue of Eqs. (16) and (18). In Fig. 2, we illustrate the real parts of the optical potentials at $\delta = 0$ for densities $\rho_B = 0.16, 0.32$, and 0.48 fm^{-3} with the NJL model and FSUGold. Note that neutron and proton Dirac optical potentials at $\delta \neq 0$ are reasonably separate for unequal proton and neutron scalar and vector densities [55], while we do not depict them in Fig. 2 for concision. At $\rho_B = 0.16$ fm^{-3}, the Dirac optical potentials of various models (FSUGold, NJL350, and NJL400) are very close to each other, because the present nuclear models are well constrained by saturation properties. Beyond saturation density, it is known that the large difference in the nuclear EOS may arise from different models. In RMF models, the difference in

the EOS can partly from moderately different scalar densities which is associated with the scalar potential. While at high densities the dropping scalar densities given by the NJL model are totally different from those given by usual RMF models due to the chiral symmetry effect, the scalar component of the optical potentials separates obviously from the one from the usual RMF models. This can be observed clearly in Fig. 2. At $\rho_B = 0.32$ fm^{-3}, which is close the critical density in NJL350, the scalar Dirac optical potential with the NJL350 shallows clearly, compared to that with the FSUGold and NJL400. As the baryon density rises further to 0.48 fm^{-3}, the chiral symmetry is already restored in NJL350, and it is partially restored in NJL400. In this case, the NJL350 has the very small scalar density, followed by the scalar density with the NJL400. As a consequence, the scalar optical potential with the NJL350 and NJL400 is clearly above the one with the FSUGold. As shown in Fig. 2, there is no difference in the vector parts of Dirac optical potentials with the NJL350, NJL400, and FSUGold, because the vector parts depend only on the same baryon density. Note that the imaginary parts of the optical potentials have the similar features as in the real parts, and we neglect the figurations for simplicity.

The nucleon SEPs, given by Eqs. (19) and (20), are depicted in Fig. 3 for symmetric nuclear matter with $\delta = 0$. We see that the nucleon SEPs are almost the same at $\rho_B = 0.16$ fm^{-3} with different models, which is consistent with the
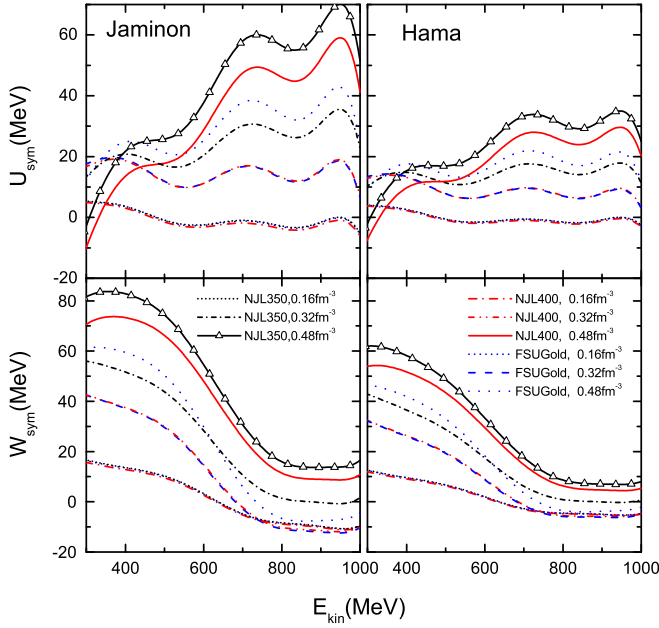
FIG. 4. The symmetry potential as a function of the nucleon kinetic energy at different densities. The differentiation of the left and right panels is similar to that in Fig. 3.

FIG. 5. The symmetry potential as a function of density at $E_{\mathrm{kin}} = 500$ and 800 MeV.

case for optical potentials, as shown in Fig. 2. The effect from the chiral symmetry starts to arise as the density increases. For instance, at $\rho_B = 0.32$ fm^{-3}, since the chiral symmetry in NJL350 is nearly restored, the real part of the nucleon SEP increases sharply due to the large restoration of chiral symmetry. A similar case takes place for the real part of the nucleon SEP with the NJL400 at $\rho_B = 0.48$ fm^{-3}, which is close to its critical density of chiral symmetry restoration. As shown in Fig. 3, the imaginary part of the nucleon SEP with the NJL model becomes lower than the one with the FSUGold, resulting from the effect of the chiral symmetry restoration. In general, the density and energy evolutions of $U_{\mathrm{sep,H}}^{\mathrm{tot}}$ and $U_{\mathrm{sep,J}}^{\mathrm{tot}}$ are similar in the two cases. However, since a factor M/E exists in the relation $U_{\mathrm{sep,H}}^{\mathrm{tot}} = U_{\mathrm{sep,J}}^{\mathrm{tot}} M/E$, a shrinkage of the SEPs in the right panels appears in comparison to those in left panels.

The symmetry potential can be simply regarded as the potential part of the symmetry energy, and the uncertainty of the symmetry energy is largely attributed to that of the symmetry potential [14,52–55]. However, the symmetry potential in RIA is rather constrained by the scattering amplitude together with densities from relativistic models. From different sources of optical potentials, the symmetry potential is extracted to be linear in the kinetic energy in the energy region below 200 MeV [14]. With the RIA, the linear dependence on the nucleon kinetic energy was approved earlier by Li *et al.* [54]. As the kinetic energy extends to the region above 400 MeV, the symmetry energy stays almost unchanged for densities in the vicinity of saturation [55]. In Fig. 4, we show the real and imaginary symmetry potentials, given by Eq. (21), as functions of nucleon kinetic energy. It is found that the U_{sym} with NJL350, NJL400, and FSUGold are close to each other at $\rho_B = 0.16$ fm^{-3}, and it is nearly constant at higher nucleon

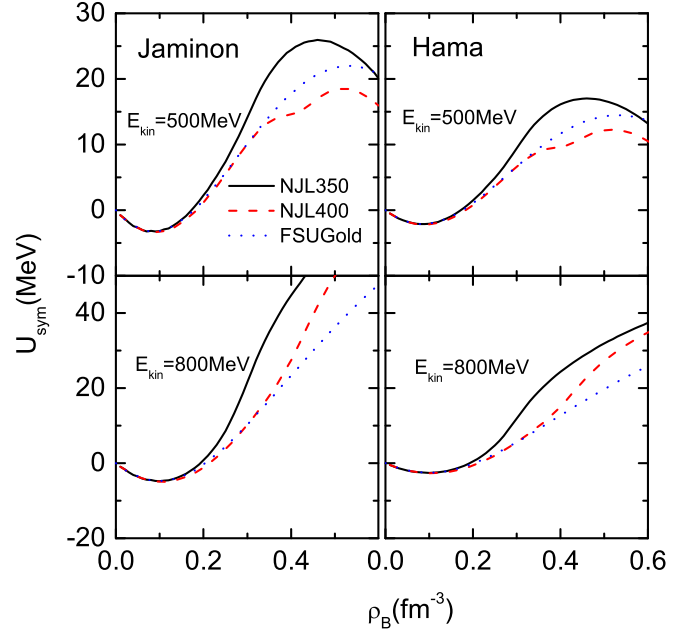kinetic energy, consistent with that in Ref. [55]. With the increase of density, the chiral symmetry effect on the symmetry potentials is just similar to that for the SEP, as can be observed by comparing Fig. 4 with Fig. 3. The difference is that at high densities the real symmetry potential, namely the Lane potential U_{sym}, fluctuates with energy that is seeded by the wavy $F_V(E_{\mathrm{kin}})$ in energy and the amplification by multiplying E_{kin} in the last term in Eq. (19). We can infer that the fluctuation is dominated by the vector potential, since it survives in the NJL results whose scalar potential is negligible near the critical density. This can be nicely verified numerically. It should be noted that the imaginary symmetry potential displays an energy dependence different from that of the real symmetry potential at a fixed density: It decreases with increasing nucleon kinetic energy. Nevertheless, the symmetry potential is largely modified by the effect of chiral symmetry restoration especially at higher energies, as shown in Fig. 4. Yet, we see that the symmetry potential relies on the approximations adopted. The shallower symmetry potentials correspond to the shallower SEPs as shown in Fig. 3.

Shown in Fig. 5 is the density profile of the Lane potential for $E_{\mathrm{kin}} = 500$ and 800 MeV. It is clearly shown that the symmetry potential becomes apart from different models with increasing density. Interestingly, when the chiral symmetry is partially restored at higher densities, the separation between those from different parametrizations appears to be large. Especially at $E_{\mathrm{kin}} = 800$ MeV, the separation actually characterizes the difference induced by the chiral symmetry restoration in the NJL model. Indeed, the difference between the NJL model and the RMF FSUGold is irrelevant to the vector potentials at a fixed density and fixed energy, and it is uniquely associated with the scalar potential (or, the scalar density) and the nucleon effective mass therein. However, the symmetry potential with the FSUGold at $E_{\mathrm{kin}} = 500$ MeV is
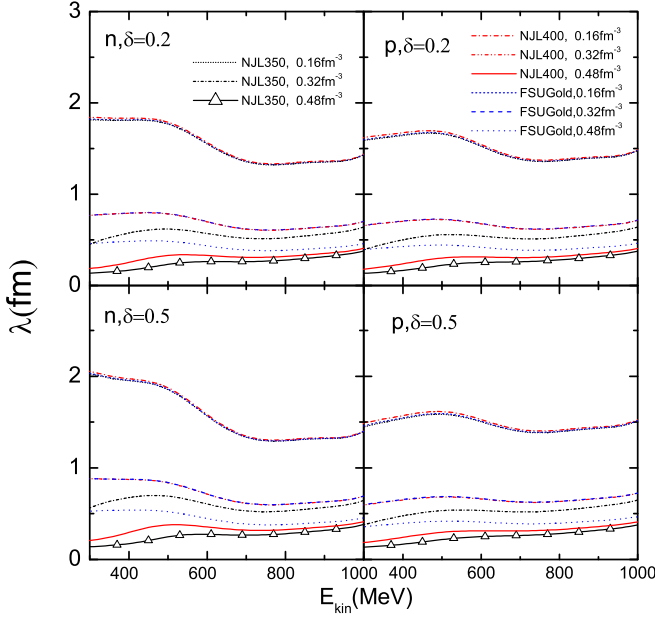
FIG. 6. The nucleon mean free path as a function of the nucleon kinetic energy for different densities with NJL350, NJL400, and FSUGold.

FIG. 7. The in-medium NN cross section as a function of the nucleon kinetic energy at densities 0.16, 0.32, and 0.48 fm^{-3}.

unusually higher than the one with the NJL400 at higher densities, as shown in the upper panel of Fig. 5. In fact, the uplift of the symmetry potential at lower energies with the FSUGold is ascribed to the cancellation between the energy-dependent terms in Eq. (19): U_S^{tot} and $U_S^{tot2}/2M$ that are opposite in sign. Though the values of U_S^{tot} and $U_S^{tot2}/2M$ are individually much larger than those given by the NJL model at higher densities, the cancellation can give rise to a value comparable to that with the NJL model. Note that this unusual uplift can be found consistently in Fig. 4 in the low-energy region. With increasing the energy, the clearly lower optical potentials do not favor a delicate cancellation anymore, resulting in a large difference induced by the chiral symmetry effect, as shown in Figs. 4 and 5, even though the SEPs are suppressed in the Hama's expression with increase of the kinetic energy; see Eq. (20).

Before addressing the in-medium NN cross sections, we present in Fig. 6 the nucleon MFPs at $\delta = 0.2$ and 0.5, calculated by Eq. (22). The MFP of a particle is the average distance traveled between two successive collisions of the particle, and here it is an input to work out the in-medium NN cross section. The nucleon MFP at high densities will be obviously shorter than that at low densities, as is consistently given in Fig. 6. It is worth noting that the restoration of chiral symmetry leads to a decrease in MFPs, caused by a sharp increase in the real SEP. For instance, at $\rho_B = 0.32$ fm^{-3}, where the chiral symmetry in NJL350 is largely restored, the nucleon MFPs with the NJL350 are lowered clearly, compared to those with the NJL400 and FSUGold. As shown in Fig. 6, the high-energy behavior of the MFPs tends to be flattened in all of the present parametrizations, although the MFPs are not a monotonous function of nucleon kinetic energy especially at high densities in the NJL model. Besides, the nucleon MFPs are dependent on the isospin; see Eq. (22). With increasing δ, the difference
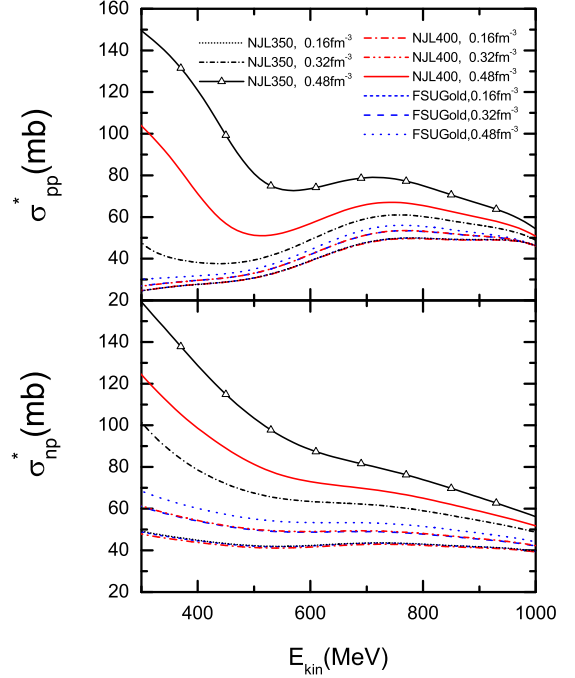
between neutron and proton MFPs becomes moderately larger [23], as shown in Fig. 6.

Now, we discuss the in-medium NN cross sections. Shown in Fig. 7 is the in-medium NN scattering cross sections as a function of kinetic energy with NJL350, NJL400, and FSUGold. Once again, we see that the overlap of the curves at saturation density for the well-constrained saturation properties of these models. As shown in the figure, the NN cross sections with the FSUGold just rise moderately with increasing the density, while the rise with the NJL350 and NJL400 can be dramatic especially at large densities close to the critical density. The large rise with the NJL model can be understood by the small scalar densities which yield small nucleon effective masses. Phenomenologically, the in-medium NN cross sections were approximately scaled down by the nucleon mass square in the medium [11] at low energies, whereas here the NN cross sections evolve upward with decreasing nucleon effective mass M^*. In the kinetic energy region where the RIA applies, the lower energy region displays a more apparent rise of σ_{pp}^* and σ_{np}^* with increasing the density, while the contraction of the rise at higher energies is consistent with the correspondingly reduced scattering amplitudes. As seen in Eq. (25), there is a difference between the σ_{np}^* and σ_{pp}^*. It is known that at low energies less than 300 MeV, the free-space σ_{np} is about three times the size of the free-space σ_{pp}. The proportion between the neutron-proton and proton-proton cross sections in the medium changes with the density and energy. As seen in Fig. 7, the in-medium cross section σ_{pp}^* develops to be above σ_{np}^* at higher energies.

The density dependences of the NN cross sections are shown in Fig. 8 for $E_{kin} = 500$ and 800 MeV. It is striking that the sharp difference in the NN cross sections appears for
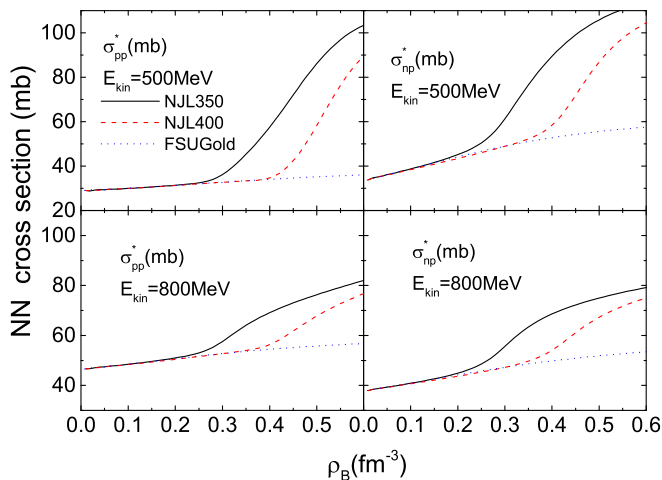
FIG. 8. The in-medium NN cross section as a function of density at $E_{\text{kin}} = 500$ and 800 MeV.

different models with increasing the density. The difference in the NN cross sections between different models is given by the scalar component of the optical potentials, since the vector optical potential in RIA is identical for different models at a fixed density and fixed energy. As seen in the left upper panel of Fig. 8, the NN cross section with the NJL model can be larger than that with the FSUGold by a factor of 3 at high densities. The results in Fig. 8 reflect a fact that the chiral symmetry restoration has a direct and clear correlation with the in-medium NN cross sections: The eclipse of the nucleon mass caused by the chiral symmetry restoration yields an apparently large rise in the in-medium NN cross sections. Not only can the chiral symmetry constrain the strong interaction, but also it can signal the internal structures of nucleons which might be encountered in the energetic heavy-ion collisions. Indeed, the original NJL model and later versions treated the hadrons as composite constituents. It has been recognized generally that the chiral phase transition coincides with the color deconfinement, evidenced by the vanishing baryon mass (from constituent mass to the current mass) [71], although quarkyonic matter between the hadron and quark phases was proposed in the recent past [72,73]. Similar role of the chiral symmetry in pointing to the internal structure ends but not in the more fundamental structure of quarks and leptons by solving the axial anomaly [74,75]. Empirically speaking, the effect produced by the chiral symmetry may roughly reflect the influence of the interior quark degrees of freedom in dense matter. In this sense, the consideration of chiral symmetry in mean-field potentials is of significance and economical for the transport models when reaching out to internal degrees of freedom in the high-density region. Indeed, the high-density region where the chiral symmetry matters was produced by the energetic heavy-ion collisions; for instance, see Refs. [3,76]. We notice that the present simple RIA should not be perfect when the in-medium effects of the pion production resonances are treated equally as the nucleons. In the low-energy region below the pion production threshold, one can deal with this issue better by extending the RIA to the relativistic Love-Franey model [51–54].

We should figure out that the increasing trend of in-medium NN cross sections with the density at high energies is different from that in the literature at low nucleon energies [15–18,20,22] and that the significance of this increasing trend is based more upon comparison to the results with the usual RMF model (FSUGold). It was familiar inadvertently that the in-medium NN cross sections decrease with increasing density at low energies. Our finding in the high-energy region, albeit different, is not unique. In fact, it was found in the Dirac-Brueckner theory that the in-medium NN cross sections can increase with the density at high nucleon momenta [24]. Note that the present relativistic treatment can result in the proximity of the NN cross sections at very low densities to the free-space limits, consistent with that in Ref. [23].

At last, it is worth noting that the symmetry potential effect on the in-medium NN cross sections is not included in the present work. The symmetry potential just has a negligible effect around the saturation density [23]. In much denser matter where the RMF works nicely, the role of the symmetry potential that is associated with the isospin-dependent Pauli blocking would be limited in the in-medium NN cross section in the case of $E_{\text{kin}} > k_F$. However, to better work out the NN cross sections in asymmetric matter, we need to develop a method to include the contribution of the symmetry potential and leave it in a future work.

IV. SUMMARY

In this work, we have studied the chiral symmetry effect in the NJL model on the symmetry potential and in-medium NN cross section based on the Dirac optical potentials in RIA. In comparison, we perform the calculation with the RMF parametrization FSUGold. We have calculated the Dirac optical potentials, the Schrödinger equivalent potentials, symmetry potentials, nucleon mean free paths, and the in-medium NN cross sections with these models. We have found that the key ingredient in RIA is the scalar density, as the vector component is identical for all models at a fixed density and a fixed nucleon kinetic energy. The scalar density obtained from the NJL model is dramatically reduced at higher densities in comparison to that with usual RMF models, because the chiral restoration in the medium leads to a vanishing nucleon effective mass in the NJL model. We have observed that the physical quantities mentioned above undergo a consistently similar variation with the evolution of nucleon density and kinetic energy.

With the chiral symmetry being restored considerably, the real part of SEPs increases sharply, and this sharp rise is transmitted to the symmetry potential. For high kinetic energies, the chiral symmetry effect on the symmetry potential can be clearly measured by the difference from the one with the FSUGold. The nucleon MFPs with the chiral symmetry model are obviously lower than those with the FSUGold, as the chiral symmetry starts to be restored partially. Correspondingly, the in-medium NN cross sections with the NJL model increases sharply for the large eclipse of the nucleon effective mass caused by the chiral symmetry restoration. In short, the in-medium NN cross sections in RIA can measure the chiral symmetry restoration. On the other hand, the in-medium NN

cross sections as a key input of the transport models should account for the chiral symmetry effect in simulating the creation of dense matter.

[1] A. Ozawa, T. Suzuki, and I. Tanihata, Nucl. Phys. A **693**, 32 (2001).

[2] J. Xu, Prog. Part. Nucl. Phys. **106**, 312 (2019).

[3] P. Danielewicz, R. Lacey, and W. G. Lynch, Science **298**, 1592 (2002).

[4] B. A. Li, B. J. Cai, L. W. Chen, and J. Xu, Prog. Part. Nucl. Phys. **99**, 29 (2018).

[5] J. M. Lattimer and M. Prakash, Science **304**, 536 (2004).

[6] A. W. Steiner, M. Prakash, J. M. Lattimer, and P. J. Ellis, Phys. Rep. **411**, 325 (2005).

[7] B. A. Li, L. W. Chen, and C. M. Ko, Phys. Rep. **464**, 113 (2008).

[8] M. B. Tsang, J. R. Stone, F. Camera, P. Danielewicz, S. Gandolfi, K. Hebeler, C. J. Horowitz, J. Lee, W. G. Lynch, Z. Kohley *et al.*, Phys. Rev. C **86**, 015803 (2012).

[9] C. J. Horowitz, E. F. Brown, Y. Kim, W. G. Lynch, R. Michaels, A. Ono, J. Piekarewicz, M. B. Tsang, and H. H. Wolter, J. Phys. G **41**, 093001 (2014).

[10] *Topical Issue on Nuclear Symmetry Energy*, edited by B. A. Li, A. Ramos, G. Verde, and I. Vidaña, special issue of Eur. Phys. J. A **50**(2) (2014).

[11] B. A. Li and L. W. Chen, Phys. Rev. C **72**, 064611 (2005).

[12] R. Chen, B. J. Cai, L. W. Chen, B. A. Li, X. H. Li, and C. Xu, Phys. Rev. C **85**, 024305 (2012).

[13] R. Wang, L. W. Chen, and Y. Zhou, Phys. Rev. C **98**, 054618 (2018).

[14] C. Xu, B. A. Li, and L. W. Chen, Phys. Rev. C **82**, 054607 (2010).

[15] D. Klakow, G. Welke, and W. Bauer, Phys. Rev. C **48**, 1982 (1993).

[16] G. Q. Li and R. Machleidt, Phys. Rev. C **48**, 1702 (1993).

[17] G. Q. Li and R. Machleidt, Phys. Rev. C **49**, 566 (1994).

[18] P. Danielewicz, Nucl. Phys. A **673**, 375 (2000).

[19] C. Fuchs, A. Faessler, and M. El-Shabshiry, Phys. Rev. C **64**, 024003 (2001).

[20] J. Y. Liu, W. J. Guo, S. J. Wang, W. Zuo, Q. Zhao, and Y. F. Yang, Phys. Rev. Lett. **86**, 975 (2001).

[21] F. Sammarruca and P. Krastev, Phys. Rev. C **73**, 014001 (2006).

[22] H. F. Zhang, Z. H. Li, U. Lombardo, P. Y. Luo, F. Sammarruca, and W. Zuo, Phys. Rev. C **76**, 054001 (2007).

[23] W. Z. Jiang, B. A. Li, and L. W. Chen, Phys. Rev. C **76**, 044604 (2007).

[24] F. Sammarruca, Eur. Phys. J. A **50**, 22 (2014).

[25] T. T. Wang, Y. G. Ma, C. J. Zhang, and Z. Q. Zhang, Phys. Rev. C **97**, 034617 (2018).

[26] R. Wang, Z. Zhang, L. W. Chen, C. M. Ko, and Y. G. Ma, Phys. Lett. B **807**, 135532 (2020).

[27] M. Gell-Mann and M. Lévy, Nuovo Cimento **16**, 705 (1960).

[28] Y. Nambu and G. Jona-Lasinio, Phys. Rev. **122**, 345 (1961).

[29] J. Boguta, Phys. Lett. B **120**, 34 (1983).

[30] S. P. Klevansky, Rev. Mod. Phys. **64**, 649 (1992).

[31] M. Buballa, Phys. Rep. **407**, 205 (2005).

[32] V. A. Miransky, M. Tanabashi, and K. Yamawaki, Phys. Lett. B **221**, 177 (1989).

[33] W. Z. Jiang, X. J. Qiu, Z. Y. Zhu, and Z. J. He, Phys. Rev. C **65**, 015210 (2001).

[34] K. Fukushima, Phys. Lett. B **591**, 277 (2004).

[35] P. Costa, H. Hansen, M. C. Ruivo, and C. A. de Sousa, Phys. Rev. D **81**, 016007 (2010).

[36] H. Kohyama, D. Kimura, and T. Inagaki, Nucl. Phys. B **896**, 682 (2015).

[37] C. M. Li, J. L. Zhang, Y. Yan, Y. F. Huang, and H. S. Zong, Phys. Rev. D **97**, 103013 (2018).

[38] V. Koch, T. S. Biro, J. Kunz, and U. Mosel, Phys. Lett. B **185**, 1 (1987).

[39] U. Vogl and W. Weise, Prog. Part. Nucl. Phys. **27**, 195 (1991).

[40] I. N. Mishustin, L. M. Satarov, and W. Greiner, Phys. Rep. **391**, 363 (2004).

[41] T. G. Lee, Y. Tsue, J. da Providencia, C. Providencia, M. Yamamura, Prog. Theor. Exp. Phys. **2013**, 013D02 (2013).

[42] H. Pais, D. P. Menezes, and C. Providencia, Phys. Rev. C **93**, 065805 (2016).

[43] S. N. Wei, W. Z. Jiang, R. Y. Yang, and D. R. Zhang, Phys. Lett. B **763**, 145 (2016).

[44] C. A. Graeff, M. D. Alloy, K. D. Marquez, C. Providencia, and D. P. Menezes, J. Cosmol. Astropart. Phys. **01**, 024 (2019).

[45] Y. J. Chen, Chin. Phys. C **43**, 035101 (2019).

[46] J. A. McNeil, L. Ray, and S. J. Wallace, Phys. Rev. C **27**, 2123 (1983).

[47] J. A. McNeil, J. R. Shepard, and S. J. Wallace, Phys. Rev. Lett. **50**, 1439 (1983).

[48] L. Ray and G. W. Hoffmann, Phys. Rev. C **31**, 538 (1985).

[49] J. P. Auger, J. Gillespie, and R. J. Lombard, Nucl. Phys. A **262**, 372 (1976).

[50] R. Klem, G. Igo, R. Talaga, A. Wriekat, H. Courant, K. Einsweiler, T. Joyce, H. Kagan, Y. Makdisi, M. Marshak, B. Mossberg, E. Peterson, K. Ruddick, and T. Walsh, Phys. Bev. Lett. **38**, 1272 (1977).

[51] C. J. Horowitz, Phys. Rev. C **31**, 1340 (1985).

[52] D. P. Murdock and C. J. Horowitz, Phys. Rev. C **35**, 1442 (1987).

[53] Z. P. Li, G. C. Hillhouse, and J. Meng, Phys. Rev. C **77**, 014001 (2008).

[54] Z. H. Li, L. W. Chen, C. M. Ko, B. A. Li, and H. R. Ma, Phys. Rev. C **74**, 044613 (2006).

[55] L. W. Chen, C. M. Ko, and B. A. Li, Phys. Rev. C **72**, 064606 (2005).

[56] J. D. Walecka, Ann. Phys. **83**, 491 (1974).

[57] J. Boguta and A. R. Bodmer, Nucl. Phys. A **292**, 413 (1977).

[58] B. D. Serot, Phys. Lett. B **86**, 146 (1979).

[59] A. R. Bodmer, Nucl. Phys. A **526**, 703 (1991)

[60] Y. Sugahara and H. Toki, Nucl. Phys. A **579**, 557 (1994).

[61] C. J. Horowitz and J. Piekarewicz, Phys. Rev. Lett. **86**, 5647 (2001).

[62] B. G. Todd-Rutel and J. Piekarewicz, Phys. Rev. Lett. **95**, 122501 (2005).

[63] S. N. Wei, R. Y. Yang, and W. Z. Jiang, Chin. Phys. C **42**, 054103 (2018).

[64] R. A. Arndt, L. D. Roper, R. A. Bryan, R. B. Clark, B. J. VerWest, and P. Signell, Phys. Rev. D **28**, 97 (1983).

[65] M. Jaminon, C. Mahaux, and P. Rochus, Nucl. Phys. A **365**, 371 (1981).

[66] S. Hama, B. C. Clark, E. D. Cooper, H. S. Sherif, and R. L. Mercer, Phys. Rev. C **41**, 2737 (1990).

[67] A. M. Lane, Nucl. Phys. **35**, 676 (1962).

[68] G. Q. Li, R. Machleidt, and Y. Z. Zhuo, Phys. Rev. C **48**, 1062 (1993).

[69] V. R. Pandharipande and S. C. Pieper, Phys. Rev. C **45**, 791 (1992).

[70] G. Q. Li and R. Machleidt, Phys. Rev. C **58**, 1393 (1998); **58**, 3153 (1998).

[71] S. R. Coleman and E. Witten, Phys. Rev. Lett. **45**, 100 (1980).

[72] P. de Forcrand and S. Kratochvila, Nucl. Phys. B (Proc. Suppl.) **153**, 62 (2006).

[73] L. McLerran and R. D. Pisarski, Nucl. Phys. A **796**, 83 (2007).

[74] J. C. Pati, A. Salam, and J. Strathdee, Phys. Lett. **B 59**, 265 (1975).

[75] G. 't Hooft, in *Recent Development in Gauge Theories* (Plenum Press, New York, 1980).

[76] W. Reisdorf, Y. Leifels, A. Andronic, R. Averbeck, V. Barret, Z. Basrak, N. Bastid, M.L. Benabderrahmane, R. Čaplar, and P. Crochet, Nucl. Phys. A **876**, 1 (2012).